Simple Tests of a Semi-Implicit Semi-Lagrangian Model on 2D Mountain Wave Problems*

JEAN-PIERRE PINTY

Laboratoire d'Aérologie, URA 354 CNRS, Université Paul-Sabatier, Toulouse, France

ROBERT BENOIT

Recherche en Prévision Numérique, Dorval, Québec, Canada

EVELYNE RICHARD

Laboratoire d'Aérologie, URA 354 CNRS, Université Paul-Sabatier, Toulouse, France

RENÉ LAPRISE

Physics Department, University of Québec at Montreal, Montreal, Québec, Canada

(Manuscript received 20 September 1994, in final form 10 February 1995)

ABSTRACT

The fully compressible 3D nonhydrostatic semi-implicit semi-Lagrangian MC2 (mesoscale compressible community) model described by Tanguay et al. has been modified in order to incorporate orography through the Gal-Chen and Somerville transformation of the vertical coordinate by Denis. In this study, a 2D version of the model is tested against classical solutions covering various mountain-wave regimes for continuously stratified flows. A close inspection of the propagation of the vertical momentum flux is performed to assess the accuracy and stability of the numerical method. The study emphasizes also the fact that a correct representation of forced hydrostatic gravity waves is reliable for Courant numbers less than 0.5. This limitation may be less severe as the flow becomes more nonhydrostatic. Furthermore, the sensitivity of the isothermal reference state for flows with realistic static stability and over steep slope mountain is explored.

1. Introduction

Primitive equations in fully compressible nonhydrostatic models are known to support undesirable fast-moving elastic wave solutions that have no relevance for meteorological applications. Under such considerations, more or less refined anelastic approximations have been introduced (Ogura and Phillips 1962; Clark 1977; Lipps and Hemler 1982; Durran 1989) to *physically* filter out such modes but at the expense of losing compressibility effects. On the other hand, the hydrostatic approximation for the vertical momentum equation that prevents the vertical propagation of unnecessary elastic waves has been widely considered at large scale and mesoscale (Pielke 1974; Anthes and Warner 1978) because it gives a considerable simplification of the numerical schemes. But since the hydrostatic set of equations still allows for horizontal propagation of external gravity waves with phase velocities comparable to that of sound waves, those models solved with explicit schemes are still facing severe time-step limitations.

In order to reconcile both compressibility and nonhydrostaticity with large time steps suitable for efficient mesoscale model integration, a category of implicit methods pioneered by Tapp and White (1976) must be considered. In their approach, these authors suggested to *numerically* filter the acoustic wave propagation by using an implicit scheme for the corresponding linear wave terms in their equations. When doing so, the maximum time-step (Δt) criterion for fully nonhydrostatic models is mostly restricted by the explicit handling of the gravity waves, that is, $\Delta t \leq 1/N$, where N is the Brunt–Väisälä frequency. Recently, noticeable progress has been made by Cullen (1990) and Tanguay et al. (1990), who demonstrated the technical feasability of handling both elastic and gravity waves in an implicit way. Furthermore, to avoid being limited by the

* This study is dedicated to Prof. André Robert, deceased 19 November 1993.

Corresponding author address: Dr. Jean-Pierre Pinty, Laboratoire de Aérologie, Université Paul Sabatier, 118 Route de Narbonne, 31062 Toulouse, Cedex, France.

advective time step, Tanguay et al. (1990) incorporated the semi-Lagrangian technique into their semi-implicit scheme. At this stage of achievement, the original setup of a semi-implicit model includes an implicit part, extracting a linearized approximation of the whole set of the compressible equations, while the explicit part gathers all the remaining terms and physical forcings. Such model constitutes a simple extension of the previous model of Robert et al. (1985) by relaxing the hydrostatic assumption.

The well-known philosophy behind implicit and Lagrangian methods is that numerical models can remain stable even for relatively large time steps. This property appears to be very attractive for large-scale models but has not yet received much interest at mesoscale because of the need to resolve accurately the gravity wave spectrum generated by orography or by thermal forcing. As pointed out by Simmons et al. (1978), semi-implicit methods can encounter numerical instabilities when they are used to integrate such high-frequency gravity wave terms at relatively high vertical resolution. The analysis given by Simmons et al. (1978) showed that the choice of the reference state around which the linear implicit section is built is of prime importance since it determines the bounds for the maximum phase speed of the resolved gravity waves. As shown by these authors, the onset of this instability seems to be independent of the choice of the time step and cannot be controlled by any classical method such as artificial wave damping. On the other hand, the Lagrangian methods have received increasing attention since the important work of Robert (1981) (see Staniforth and Côté 1991 for a review). Recently, Smolarkiewicz and Pudykiewicz (1992) were the first to illustrate the efficiency of the technique for a simple nonlinear hydrostatic 2D flow. They also stressed the importance of the averaging procedure to integrate the forcing terms along the Lagrangian trajectories in the case of a three-time-level temporal scheme.

Our purpose is to show that combining a semi-Lagrangian advection scheme with a semi-implicit temporal scheme (imposed by the treatment of the fast-oscillating linear terms in a fully compressible nonhydrostatic model) is still reliable and successful for gravity wave phenomena, despite the reservations raised by Coiffier et al. (1987) when the time step is unreasonably large. Here we use an updated version of the nonhydrostatic model of Tanguay et al. (1990) and Denis (1990) to simulate a variety of 2D flows over simple shape topography with moderately large time steps. The latter are indeed significantly larger than those used in traditional anelastic and split-explicit models running at the same scale. All the numerical experiments reported here were made with an earlier 2D version of the MC2 (mesoscale compressible community) code.[1]

[1] An updated 3D version of MC2 is available from R. Benoit, RPN, Dorval, Québec H9P 1J3, Canada.

The paper is organized as follows. The next section provides a short recall of the numerical technique used in the model. In section 3, we present a brief analysis on the maximum time step allowable for gravity wave problems. In section 4, the numerical results of mountain-wave experiments are analyzed. Several flow regimes (linear or not, hydrostatic or not) are tested for single-layered atmospheres. Concluding remarks are given in the last section.

2. Model description

a. Set of equations

The original three-dimensional nonhydrostatic model of Tanguay et al. (1990) has been modified to include the complex terrain surface condition (Denis 1990). In a projected Cartesian reference frame and with the local vertical Gal-Chen and Somerville (1975) transformation, the set of Euler equations (see also Bergeron et al. 1994) is written as

$$\frac{dU}{dt} = +fV - K\frac{\partial S}{\partial X} - RT\left(\frac{\partial q}{\partial X} + \frac{G_1}{G_0}\frac{\partial q}{\partial Z}\right) + F_U, \tag{1}$$

$$\frac{dV}{dt} = -fU - K\frac{\partial S}{\partial Y} - RT\left(\frac{\partial q}{\partial Y} + \frac{G_2}{G_0}\frac{\partial q}{\partial Z}\right) + F_V, \tag{2}$$

$$\frac{dw}{dt} = -g - \frac{RT}{G_0}\frac{\partial q}{\partial Z} + F_w, \tag{3}$$

$$(1-\alpha)\frac{dq}{dt} = -S\left(\frac{\partial U}{\partial X} + \frac{\partial V}{\partial Y}\right) - S\left[\frac{G_1U + G_2V}{G_0(H-Z)}\right] - \frac{1}{G_0}\left[\frac{\partial (G_0W)}{\partial Z}\right] + \frac{F_T}{T}, \tag{4}$$

$$\frac{dT}{dt} = \alpha T\frac{dq}{dt} + F_T, \tag{5}$$

$$W = \frac{S(G_1U + G_2V) + w}{G_0}. \tag{6}$$

In these equations the symbols have their usual meaning or have been defined in Tanguay et al. (1990). We just recall that $q = \ln(p/p_0)$, where p_0 is a constant, $\alpha = R/C_p$, where R and C_p are the gas constant and heat capacity at constant pressure, $K = (U^2 + V^2)/2$, and S is the map factor for a conformal projection from the sphere to the local Cartesian reference frame. Terms F_U, F_V, F_w, and F_T are the source terms of momentum and the diabatic heating, respectively. The only differences of the model equations with that of Tanguay et al. (1990) are the introduction of the generalized vertical velocity $W = dZ/dt$, the splitting of the horizontal pressure gradients into two terms, and the presence of the G_i's metric factors. By definition, the Gal-Chen and

Somerville terrain-following coordinate projects the (x, y, z) system of equations into a (X, Y, Z) reference frame with

$$X = x, \quad Y = y, \quad Z = H\left[\frac{z - h_0(X, Y)}{H - h_0(X, Y)}\right] \tag{7}$$

and

$$\frac{\partial Z}{\partial X} = \frac{G_1}{G_0}, \quad \frac{\partial Z}{\partial Y} = \frac{G_2}{G_0}, \quad \frac{\partial Z}{\partial z} = \frac{1}{G_0}. \tag{8}$$

The analytical expressions of the G_i's metric factors are straightforward and can be found in Denis (1990) or Bergeron et al. (1994).

In order to decompose the system for equations (1)–(6) into an implicit and an explicit part, it is necessary to define a hydrostatic reference state (T^* and q^*) around which the thermal vertical structure of the atmosphere is expanded ($T = T^* + T'$ and $q = q^* + q'$). A stable state is chosen because it allows for the implicit treatment of the gravity waves. An isothermal state is generally chosen because of the stability it confers to the semi-implicit scheme (Simmons et al. 1978). Conversely, as indicated by Tanguay et al. (1990), an isentropic reference state would isolate only the acoustic wave components as in Tapp and White (1976). So we use $T^* = \text{const}$ and $q^*(z) = q_0^* - gz/RT^*$ with $q_0^* = 0$ for convenience. Consequently, (1)–(6) are now recast in the following form:

$$\frac{DU}{Dt} + RT^* \frac{\partial q'}{\partial X} = r_1, \tag{9}$$

$$\frac{DV}{Dt} + RT^* \frac{\partial q'}{\partial Y} = r_2, \tag{10}$$

$$\frac{Dw}{Dt} + \frac{RT^*}{G_0}\frac{\partial q'}{\partial Z} - g\frac{T'}{T^*} = r_3, \tag{11}$$

$$(1 - \alpha)\left(\frac{Dq'}{Dt} - \frac{gw}{RT^*}\right) + S\left(\frac{\partial U}{\partial X} + \frac{\partial V}{\partial Y}\right) + \frac{1}{G_0}\frac{\partial (G_0 W)}{\partial Z} = r_4, \tag{12}$$

$$\frac{DT'}{Dt} - \alpha T^*\left(\frac{Dq'}{Dt} - \frac{gw}{RT^*}\right) = r_5, \tag{13}$$

$$w - G_0 W = r_6, \tag{14}$$

with

$$r_1 = -RT'\frac{\partial q'}{\partial X} - RT\frac{G_1}{G_0}\frac{\partial q'}{\partial Z} - W\frac{\partial U}{\partial Z} + fV - K\frac{\partial S}{\partial X} + F_U, \tag{15}$$

$$r_2 = -RT'\frac{\partial q'}{\partial Y} - RT\frac{G_2}{G_0}\frac{\partial q'}{\partial Z} - W\frac{\partial V}{\partial Z} - fU - K\frac{\partial S}{\partial Y} + F_V, \tag{16}$$

$$r_3 = -RT'\frac{1}{G_0}\frac{\partial q'}{\partial Z} - W\frac{\partial W}{\partial Z} + F_w, \tag{17}$$

$$r_4 = -S\left[\frac{G_1 U + G_2 V}{G_0(H - Z)}\right] - (1 - \alpha)W\frac{\partial q'}{\partial Z} + \frac{F_T}{T}, \tag{18}$$

$$r_5 = \left(\frac{\alpha T'}{1 - \alpha}\right)\left\{-S\left(\frac{\partial U}{\partial X} + \frac{\partial V}{\partial Y}\right) - S\left[\frac{G_1 U + G_2 V}{G_0(H - Z)}\right] - \frac{\partial W}{\partial Z}\right\} - W\frac{\partial (T' - \alpha T^* q')}{\partial Z} + \left[\frac{T - \alpha T^*}{T(1 - \alpha)}\right]F_T, \tag{19}$$

$$r_6 = -S(G_1 U + G_2 V). \tag{20}$$

Notice that now the 2D Lagrangian derivative is defined on the Z surfaces as

$$\frac{D}{Dt} = \frac{\partial}{\partial t} + S\left(U\frac{\partial}{\partial X} + V\frac{\partial}{\partial Y}\right). \tag{21}$$

As indicated in (15)–(20), the vertical advection is still being done with an Eulerian scheme in this early variant of the MC2 model.

b. Numerical integration

An Arakawa C grid is used in the horizontal and a Tokioka B grid (Tokioka 1978) in the vertical (see Haltiner and Williams 1980).

The temporal scheme differs slightly from the original one of Tanguay et al. (1990) because it takes advantage of spatially averaging the explicit nonlinear terms [r_i's in (15)–(20)] as shown by Tanguay et al. (1992). With Ψ standing for any of the six model variables,[2] the set of model equations can be rewritten symbolically as

$$\frac{D\Psi}{Dt} + \mathcal{L}_I(\Psi) = \mathcal{N}_E(\Psi), \tag{22}$$

where $\mathcal{L}_I(\Psi)$ identifies the linear implicit forcing terms that are time- and space-averaged along the Lagrangian trajectories, while $\mathcal{N}_E(\Psi)$ stands for the nonlinear explicit contributions ($\equiv r_i$'s) that are time centered and

[2] In the diagnostic equation (6), the contravariant vertical velocity W is indeed considered a prognostic variable because it is time averaged by the implicit scheme.

space averaged. Application of the semi-implicit semi-Lagrangian scheme leads to the following temporal discretization

$$\Psi^{t+\Delta t}_{X,Y,Z} + \Delta t[\mathcal{L}_I(\Psi^{t+\Delta t}_{X,Y,Z})] = \Psi^{t-\Delta t}_{X-2\alpha,Y-2b,Z} - \Delta t[\mathcal{L}_I(\Psi^{t-\Delta t}_{X-2\alpha,Y-2b,Z})] + \Delta t[\mathcal{N}_E(\Psi^{t}_{X,Y,Z}) + \mathcal{N}_E(\Psi^{t}_{X-2\alpha,Y-2b,Z})]. \quad (23)$$

The Lagrangian displacements a and b are computed iteratively at midtrajectory location as in Robert et al. (1985). The elimination procedure of the implicit variables $\Psi^{t+\Delta t}_{X,Y,Z}$ leads to a 3D Helmholtz equation to be solved for $q'^{t+\Delta t}_{X,Y,Z}$:

$$\left(\mathcal{H} + \Delta t^2 \frac{\alpha g^2}{RT^*}\right)[(1-\alpha) - \Delta t^2 RT^* S\nabla^2](q'^{t+\Delta t}_{X,Y,Z}) - \Delta t^2 RT^*\{\mathcal{D}_2[\mathcal{D}_1(q'^{t+\Delta t}_{X,Y,Z})]\} = F(X, Y, Z; t, t-\Delta t). \quad (24)$$

Here $F(X, Y, Z; t, t-\Delta t)$ is a complicated expression that contains all the residues coming from the right-hand side of (23), while the discrete operators $\mathcal{D}_1$ and $\mathcal{D}_2$ have the formal definitions:

$$\mathcal{D}_1(\Psi) = \frac{1}{G_0}\frac{\partial \Psi}{\partial Z} - \frac{\alpha g}{RT^*}\bar{\Psi}^Z, \quad (25)$$

$$\mathcal{D}_2(G_0\Psi) = \frac{1}{G_0}\frac{\partial G_0\Psi}{\partial Z} - \frac{(1-\alpha)g}{RT^*}\overline{G_0\Psi}^Z, \quad (26)$$

where $(^{-Z})$ denotes a vertical average. Notice that $\mathcal{H}$ flags the hydrostatic approximation in (24), that is, $\mathcal{H} = 0$ when $dw/dt - F_w = 0$ in (3) but $\mathcal{H} = 1$ otherwise.

The solution of the nonsymmetric equation (24) is easily obtained via an efficient factorized 3D-ADI method with a quasi-optimal converging coefficient set. The boundary conditions are such that $W = 0$ at the top and the bottom of the domain; at the lateral boundaries, a sponge zone, with a blending coefficient varying as a sine-square function, is provided for the dynamical fields. Given the $q'^{t+\Delta t}_{X,Y,Z}$ solution of (24), the update of the other model variables at $t + \Delta t$ is straightforward and proceeds as in Tanguay et al. (1990), but for the adopted Z vertically transformed set of equations (9)–(14). Finally a weak running time filter (Robert 1966) is applied to prevent decoupling of the odd and even time steps. All the details concerning the method of solution for the discretized problem can be found in Bergeron et al. (1994).

3. Mathematical analysis of the discrete scheme

The semi-implicit semi-Lagrangian integration of the numerical model guarantees a good stability of the solutions at large scale provided a sufficiently stable reference state is chosen (Simmons et al. 1978). This is the major advantage of such technique over explicit Eulerian methods that possess a strong limitation of their time step. At mesoscale, however, the time-step requirement is not so crucial because of the short timescale of many of the parameterized physical processes. Here the need of an accurate resolution of fast-moving gravity waves is of prime importance, and hence the response of the numerical scheme needs to be examined in detail.

a. The semi-implicit scheme

It is well known that an implicit scheme is unconditionally stable for the integration of a linearized set of equations because it slows the phase speed of the gravity waves when long time steps are used. For instance, Tanguay et al. (1990) showed that for a nonadvecting flow, the local true frequency Ω_T of a wave is related to its numerical counterpart Ω by the relation $\Omega = (\Delta t)^{-1}\tan^{-1}(\Omega_T \Delta t)$, which has always real solutions for Ω regardless of the value of Δt. For comparison, the derivation of the equivalent relation for a fully explicit scheme gives $\Omega = (\Delta t)^{-1}\sin^{-1}(\Omega_T\Delta t)$ (Haltiner and Williams 1980), but now the wave speed is increased and the stability criterion is $\Delta t < 1/\Omega_T$. Whereas both implicit and explicit schemes are second-order accurate, it should be noted that when the phase angle $\Omega_T\Delta t$ is less than 0.78, the accuracy of the explicit scheme is better.

The temporal scheme used to integrate the system (9)–(14) is semi-implicit because the nonlinear terms in the right-hand side are treated with a classical explicit leapfrog scheme. The partitioning between the implicit and explicit components is formally determined by the choice of the reference state, which in turn determines the maximum gravity wave speed in the implicit integration. Because of its stability and simplicity (Simmons et al. 1978), the isothermal reference state was chosen, but at the expense of accuracy when the ambient stratification is considerably reduced (as in real atmosphere) as well as the corresponding maximum gravity wave speed requirement. It can be speculated that when there is a great departure of stability between the reference and the actual tropospheric states, the retardation of the wave motion due to the implicit treatment of the linear part might be excessive for nonstationary gravity wave problems. It is clear, however, that tuning (here, lowering) the stability of the reference state might be an appropriate way to preserve both stability and accuracy of the semi-implicit scheme. Although this question is beyond the scope of the present study where we only attempt to test the model on stationary mountain wave problems, the behavior of flows with reduced stability is examined in section 4b.

b. The semi-Lagrangian advection

As the analysis of mountain waves can be done by considering a simplified set of equations with little loss

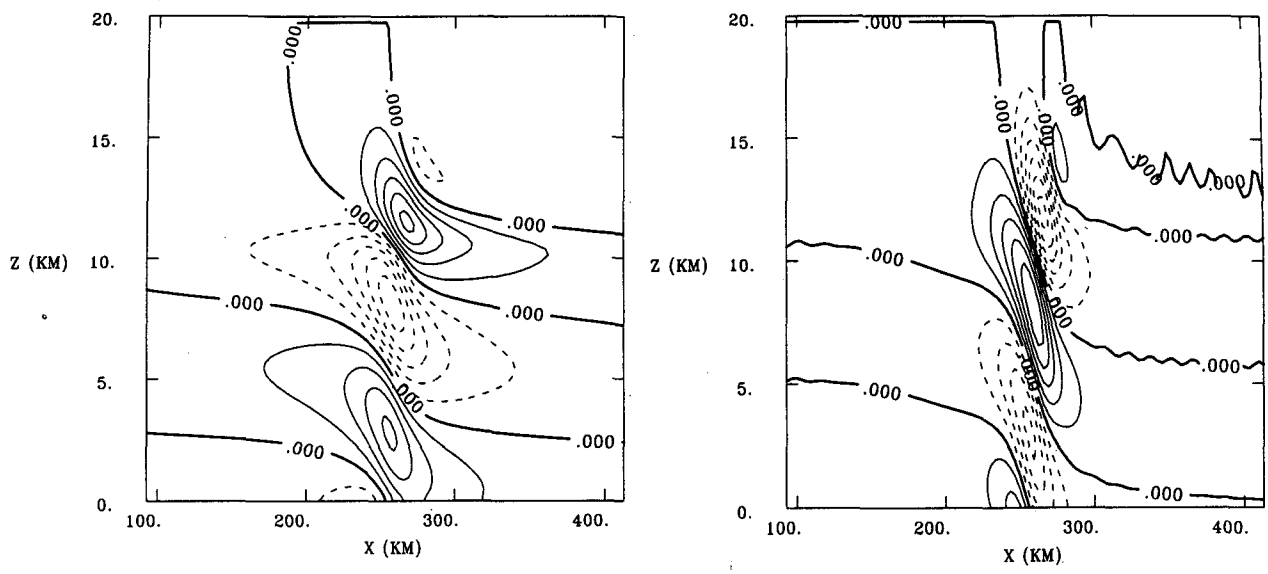

FIG. 1. Hydrostatic linear isothermal case with $U_0 = 32$ m s^{-1} at $t^* = 80$: (a) horizontal wind perturbations (between -0.028 and 0.026 m s^{-1}) with contour interval of 0.005 m s^{-1} and (b) vertical velocities (between -0.32 and 0.29 cm s^{-1}) with contour interval of 0.05 cm s^{-1}. The dashed lines indicate negative values.

in accuracy, we use a linear implicit model with the isothermal reference state for our purpose. Ignoring the vertical Z transform and after application of the semi-Lagrangian scheme, the 2D working set of equations collapses to (see also the appendix in Tanguay et al. 1990)

$$\frac{DU'}{Dt} + RT^* \overline{\frac{\partial q'}{\partial x}}' = 0, \tag{27}$$

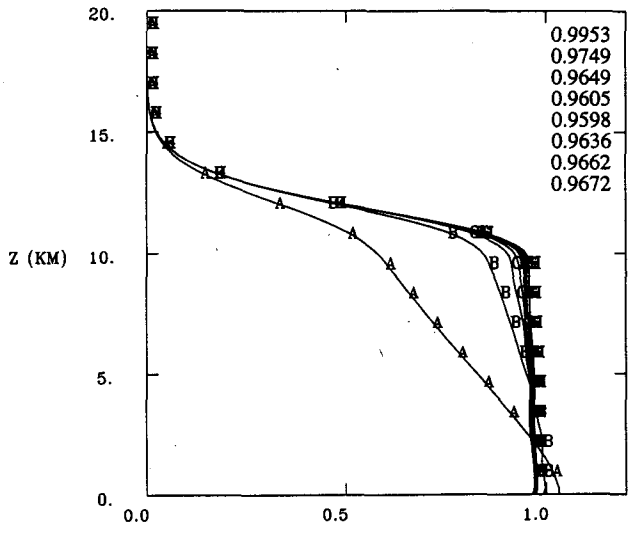

FIG. 2. Normalized vertical fluxes of momentum for the hydrostatic linear isothermal case of Fig. 1. The curve labeled A is for $t^* = 10$ and so on up to $t^* = 80$ for curve labeled H. The normalized surface pressure drag value at each $t^* = 10$ is tabulated in the upper right of the plot.

$$\frac{Dw}{Dt} + RT^* \overline{\frac{\partial q'}{\partial z}}' - g\overline{\frac{T'}{T^*}}' = 0, \tag{28}$$

$$(1-\alpha)\left(\frac{Dq'}{Dt} - \frac{g\bar{w}'}{RT^*}\right) + \left(\overline{\frac{\partial U'}{\partial x} + \frac{\partial w}{\partial z}}\right)' = 0, \tag{29}$$

$$\frac{DT'}{Dt} - \alpha T^*\left(\frac{Dq'}{Dt} - \frac{g\bar{w}'}{RT^*}\right) = 0, \tag{30}$$

where the total derivative (D/Dt) includes only a background wind $\bar{U}$ as

$$\frac{D}{Dt} = \frac{\partial}{\partial t} + \bar{U}\frac{\partial}{\partial x}, \tag{31}$$

and where the $(^{-\prime})$ average is made along the Lagrangian trajectory.

In the above system (27)–(31), a nontrivial solution of the form $F(x, z, t) = \hat{F} \exp(gz/2RT^*) \times \exp[i(kx + mz - \Omega t)]$ leads to the following discrete gravity wave dispersion relationship for stationary gravity waves ($\Omega = 0$):

$$m^2\left[\frac{\sin(m\Delta z/2)}{m\Delta z/2}\right]^2 = \frac{N^2}{\bar{U}^2}\left[\frac{\sin(k\Delta x/2)}{k\Delta x/2}\right]^2 \times \left[\frac{k\mathcal{C}\Delta x}{\tan(k\mathcal{C}\Delta x)}\right]^2 - k^2\left[\frac{\sin(k\Delta x/2)}{k\Delta x/2}\right]^2, \tag{32}$$

with the Courant number definition $\mathcal{C} = \bar{U}\Delta t/\Delta x$. At high resolution when both Δx and Δz tend to zero, the

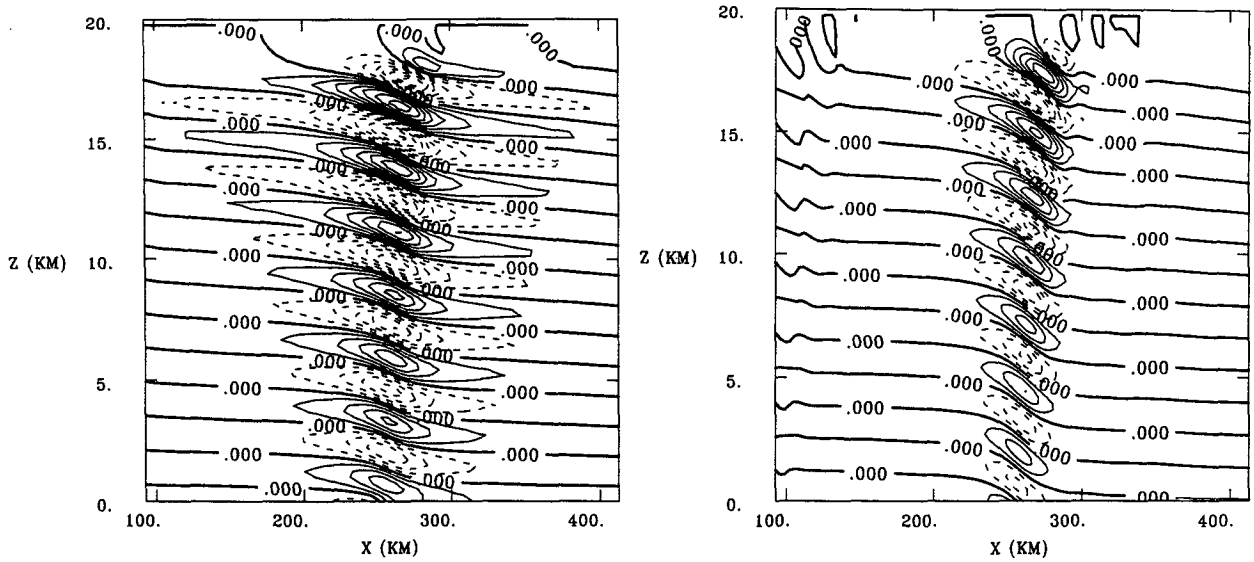

FIG. 3. Hydrostatic linear isothermal case with $U_0 = 8$ m s^{-1} at $t^* = 160$: (a) horizontal wind perturbations (between -0.036 and 0.038 m s^{-1}) with contour interval of 0.005 m s^{-1} and (b) vertical velocities (between -0.12 and 0.12 cm s^{-1}) with contour interval of 0.025 cm s^{-1}. The dashed lines indicate negative values.

classical Boussinesq gravity wave phase relationship is recovered:

$$m^2 = \frac{N^2}{\bar{U}^2} - k^2. \tag{33}$$

The comparison between the last two relations shows that the semi-Lagrangian scheme tends to reduce the intrinsic atmospheric frequency N as $\mathcal{C}$ increases. The consequence of this is fully analyzed by Héreil and Laprise (1994), who demonstrate that running with a high $\mathcal{C}$ is equivalent to shifting the higher k components of vertically propagating internal waves into the vertically trapped, evanescent regime, as is the case for nonhydrostatic flows where some wavenumbers are greater than $N/\bar{U}$. For instance, if we look to the highest-resolved horizontal wavenumber $k_{\max} = \pi/\Delta x$, (33) indicates that the corresponding vertical component m is nonevanescent whenever

$$\frac{\lambda_H}{2}\frac{1}{\Delta x} < \left|\frac{\pi\mathcal{C}}{\tan(\pi\mathcal{C})}\right| < \frac{\lambda_H}{2}\left[\left(\frac{1}{\Delta x}\right)^2 + \left(\frac{1}{\Delta z}\right)^2\right]^{1/2}, \tag{34}$$

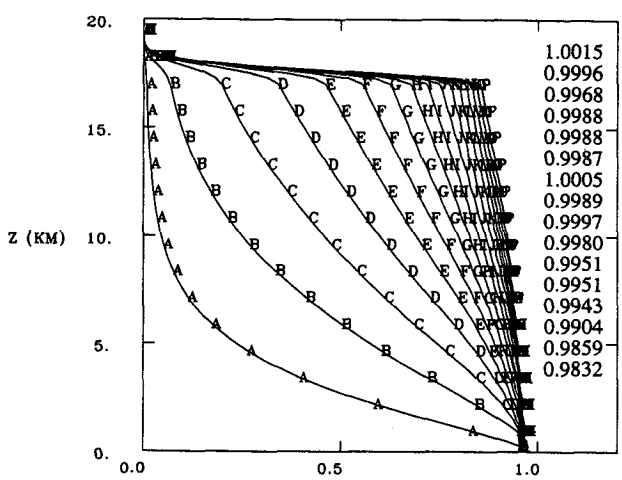

FIG. 4. Normalized vertical fluxes of momentum for the hydrostatic linear isothermal case of Fig. 3. The curve labeled A is for $t^* = 10$ and so on up to $t^* = 160$ for curve labeled P. The normalized surface pressure drag value at each $t^* = 10$ is tabulated in the upper right of the plot.

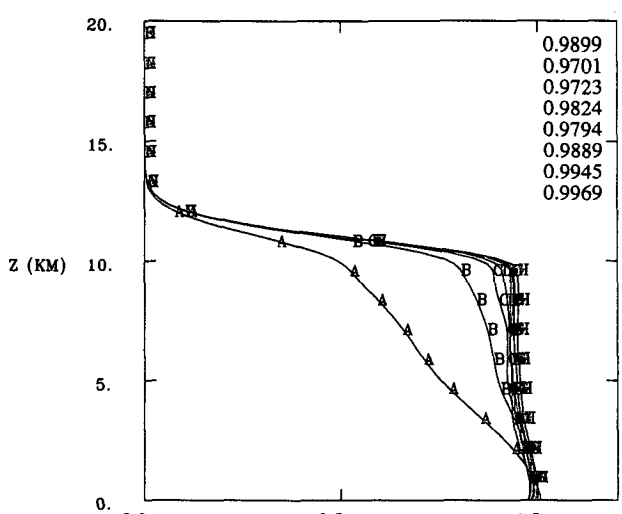

FIG. 5. As in Fig. 2 but for the hydrostatic linear case with $N = 0.01$ s^{-1} and $U_0 = 16$ m s^{-1}.

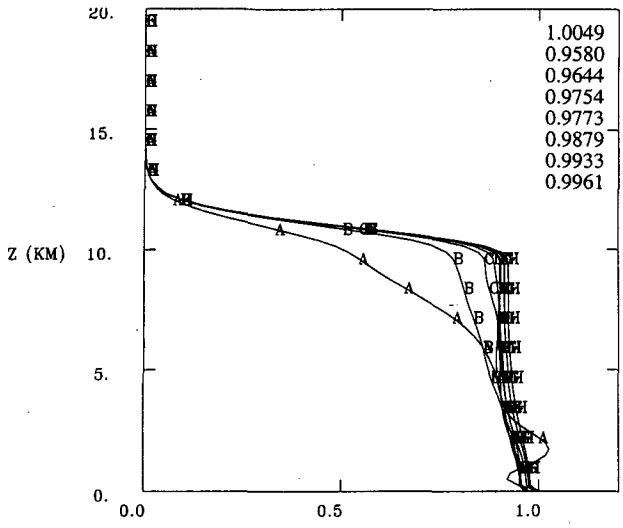

FIG. 6. As in Fig. 5 but when the isothermal reference state is $T^* = 293$ K.

where $\lambda_H = 2\pi\bar{U}/N$ corresponds to the hydrostatic vertical wavelength. The first unequality recalls that for nonhydrostatic flows, the propagation of the shortest wavelength components can be damped if the horizontal scale is smaller than λ_H. The second restriction is purely numerical, and it holds despite the fact that for hydrostatic flow gravity waves should be freely propagating. Considering that $\Delta x \gg \Delta z$ for such case, a simple numerical application of (34) indicates that there is an upper bound for the Courant number expressed by $C_{\max} \sim 0.646$ for the shortest resolved waves in the vertical, that is, $\lambda_H = 2\Delta z$. A better vertical resolution, however, allows for $C_{\max}$ to approach unity from below. It is for this reason that the numerical results of the present study will be performed with $\mathcal{C}$ lower than or equal to 0.5 in order to preserve reasonably well the dispersion relation of internal gravity waves. An intuitive geometrical interpretation of this Courant number limitation can be found by noting that when the Lagrangian paths exceed the Eulerian grid size, the averaging of scale-dependent terms such as pressure gradient terms by the semi-Lagrangian implicit scheme leads to an undesirable spatial filtering of these terms.

4. Numerical results for continuously stratified flows

a. Model setup

In order to properly simulate flows with vertically propagating internal gravity waves, the top boundary condition has to be designed carefully to allow for energy to escape out of the domain of interest (Klemp and Durran 1983). As generally done, the reflective nature of the lid condition $W = 0$ is efficiently masked by inserting a thick sponge zone below the top to absorb incident wave energy. The best results were obtained by using

$$\Psi^{t+\Delta t}_{X,Y,Z} = (1 - \beta)\Psi^{(*)t+\Delta t}_{X,Y,Z} + \beta\tilde{\Psi}_{X_0,Y_0,Z}, \quad (35)$$

where $\tilde{\Psi}_{X_0,Y_0,Z}$ is an externally prescribed value for $\Psi_{X,Y,Z}$ (here, the upstream initial sounding), $\Psi^{(*)t+\Delta t}_{X,Y,Z}$ is the model variable just after the update step, and $\beta = \beta_V$ is defined by

$$\beta_V = \begin{cases} \left(\dfrac{Z - Z_{\min}}{H - Z_{\min}}\right)^2, & Z_{\min} < Z < H, \\ 0, & \text{otherwise.} \end{cases} \quad (36)$$

This vertical profile of the damping coefficient is much simpler and gives slightly better results than that recommended by Klemp and Lilly (1978). Furthermore, it was found that accurate results were obtained by taking the thickness of the sponge zone $H - Z_{\min}$ equal to the dominant vertical wavelength of the gravity waves.

A similar sponge zone was inserted at the lateral boundaries but with $\beta = \beta_H$ [Eq. (35)] given by

$$\beta_H = \begin{cases} \cos^2\left[\dfrac{\pi}{2}\left(\dfrac{x}{x_{\text{bound}}}\right)\right], & 0 < x < x_{\text{bound}}, \\ \cos^2\left[\dfrac{\pi}{2}\left(\dfrac{L_x - x_{\text{bound}}}{x_{\text{bound}}}\right)\right], & \\ \qquad L_x - x_{\text{bound}} < x < L_x, & \\ 0, \quad \text{otherwise,} & \end{cases} \quad (37)$$

where L_x is the horizontal extension of the domain. The sponge width x_{bound} is twice the wavelength associated to the horizontal-scale perturbation approximately. Pre-

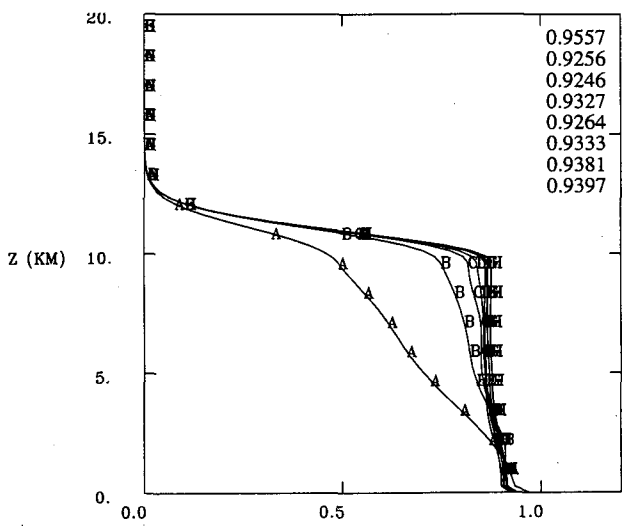

FIG. 7. As in Fig. 5 but when the isothermal reference state is $T^* = 253$ K.

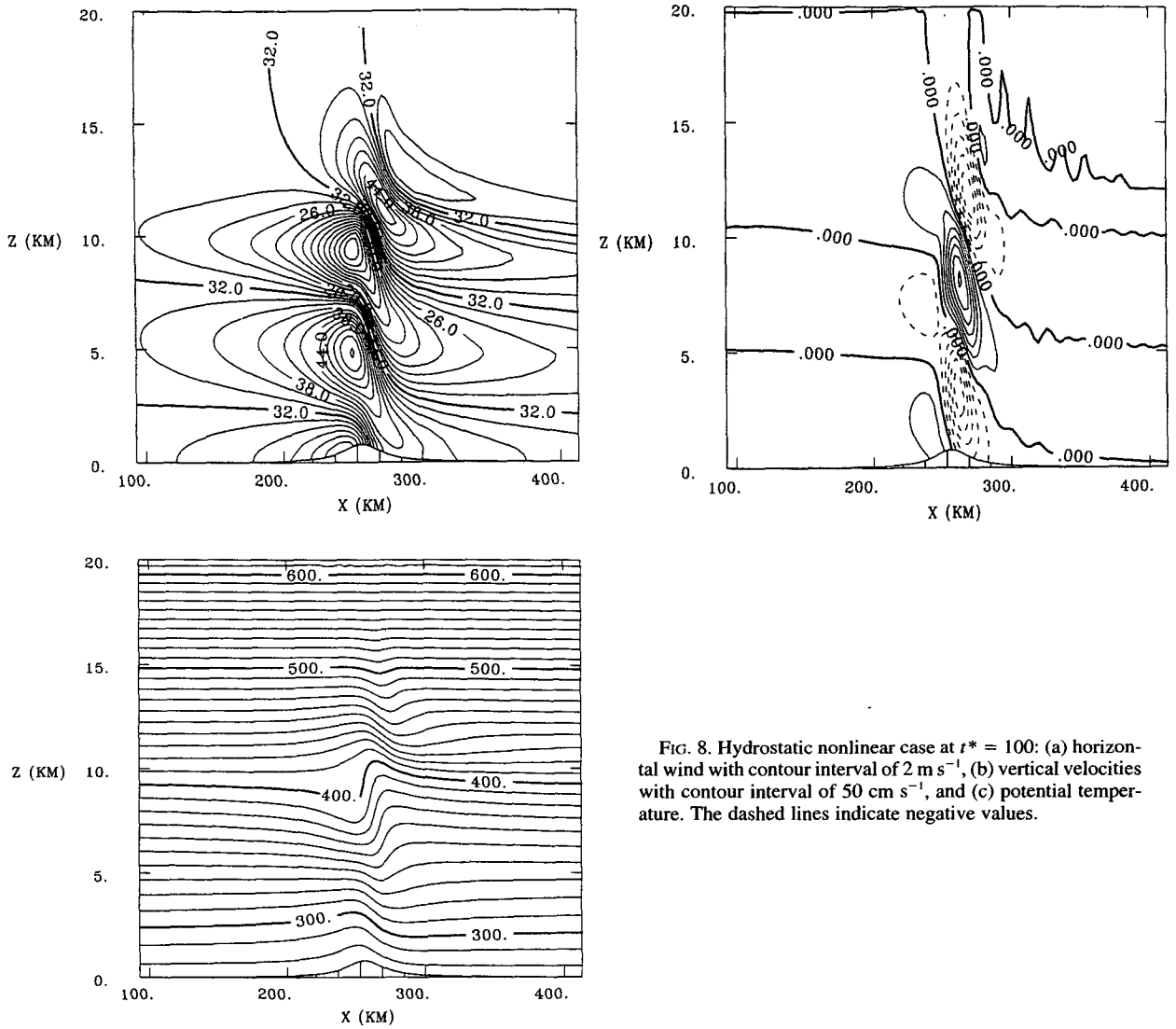

FIG. 8. Hydrostatic nonlinear case at $t^* = 100$: (a) horizontal wind with contour interval of 2 m s^{-1}, (b) vertical velocities with contour interval of 50 cm s^{-1}, and (c) potential temperature. The dashed lines indicate negative values.

liminary experiments lead us to conclude that it is better to consider $\beta_H \neq 0$ for the U, V, and w fields only.

In the following 2D numerical experiments, the profile of the symmetrical Witch of Agnesi mountain is used as described by

$$h_0(x, y) = \frac{h}{1 + (x/a)^2}, \tag{38}$$

with h the height and a the half-width of the mountain. The computational domain has 161 horizontal grid points and 81 equally spaced vertical levels. Unless specified, the time step is such that the Courant number formed with the background wind speed is 0.5. It is obvious that running with $\mathcal{C}$ equal to a multiple of 0.5 is the best situation for the Lagrangian scheme because the upstream positions ($X - 2a$ and $Y - 2b$) taken at $t - \Delta t$ are close to the gridpoint locations, and so the interpolated fields in (23) have the best accuracy. The last point to mention about the 2D version of the model is the need to modify slightly the ADI solver in order to make it suitable to integrate the Helmholtz equation (24) over a single vertical plane.

Unless otherwise stated, the integrations shown below were obtained by abruptly inserting the mountain at its full height in the initially horizontal flow.

b. *Hydrostatic waves*

In order to explore first the linear hydrostatic regime, we set $h = 1$ m and $a = 16$ km. The horizontal resolution is $\Delta X = 3.2$ km, and the highest model level is at the altitude $H = 20$ km.

1) LINEAR ISOTHERMAL CASES

Upstream conditions for the model are $T_0(=T^*) = 273.16$ K and $U_0 = 32$ m s^{-1}, thus providing one

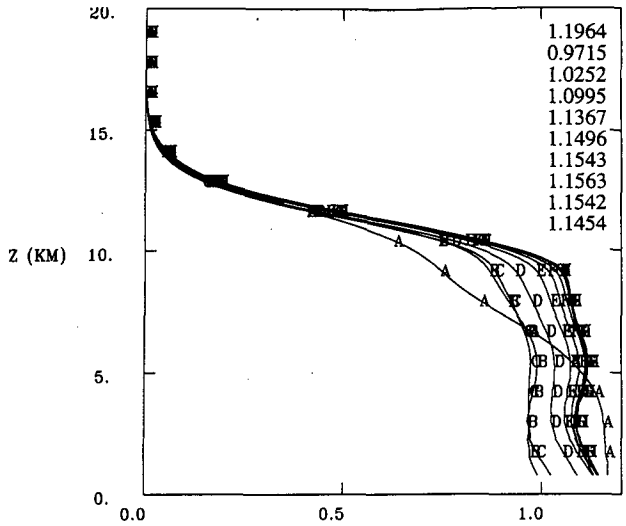

FIG. 9. Normalized vertical fluxes of momentum for the hydrostatic nonlinear case of Fig. 8. The curve labeled A is for $t^* = 10$ and so on up to $t^* = 100$ for curve labeled J. The normalized surface pressure drag value at each $t^* = 10$ is tabulated in the upper right of the plot.

fully resolved wavelength approximately as illustrated in Fig. 1 where the quasi-steady state of the wind pertubation $U' = U - U_0$ and of the vertical velocity is reproduced at $t^* = tU_0/a = 80$. The vertical flux of horizontal momentum, normalized by the theoretical wave-drag value, is plotted in Fig. 2 for regularly spaced times $\Delta t^* = 10$. The most striking feature is the good accuracy and stability of the flux that reaches the value of 0.97 over the whole undamped region. This value is in accordance with the results of Klemp and Durran (1983) and also with the computed surface pressure drag of the model within 1%. The rapid buildup of the flux with a slight early overshoot in the very low levels corresponds to the rapid propagation of the wave energy (Klemp and Lilly 1980) when the startup is abrupt; that is, the obstacle is inserted at once in an initially horizontal flow field. We believe that the somewhat rapid verticalization of the flux profiles (which never exceed the low-level values) is achieved because of the time-implicit integration of most of the perturbation for this case.

For the next experiment, the model is rerun with $U_0 = 8$ m s^{-1}, and the results are examined at $t^* = 160$. As expected, a train of waves with a shorter wavelength (and reduced numerical resolution) is formed as indicated by the horizontal and vertical wind perturbations in Fig. 3. For this simulation, the sponge layer has been greatly reduced as its thickness is taken as one vertical wavelength of the perturbation ($\lambda_H = 2\pi U_0/N$). The non-Boussinesq upward amplification of the waves proportional to $\rho_0^{-1/2}$ now becomes apparent in Fig. 3. The examination of the successive normalized vertical fluxes of momentum plotted in Fig. 4 reveals that the time taken for the solution to reach a quasi-stationary state, corresponding to a quasi-vertical profile, is relatively long. This is because the group velocity of the vertically propagating gravity waves, C_{gz}, which is proportional to U^2 (Klemp and Lilly 1980), has been greatly reduced compared to the previous simulation. Normalizing the duration of the integration by the time required for the energy of the dominant mode (that is $t^{**} = tC_{gz}/Z_{\min}$) to propagate in the "free" atmosphere, one obtains $t^{**} \sim 4$, which is lower than the

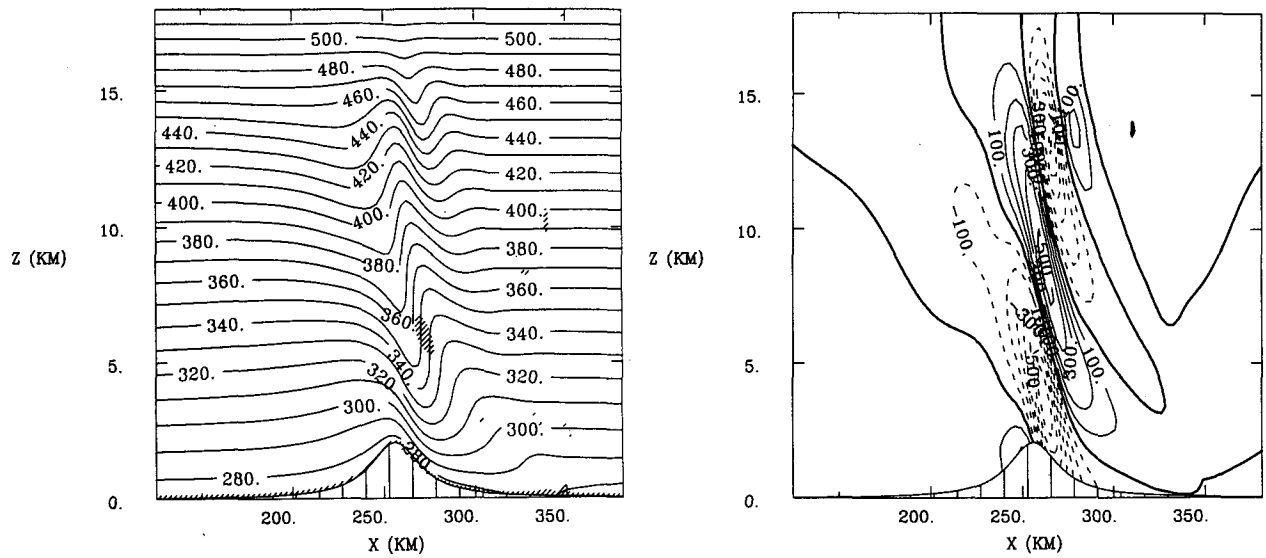

FIG. 10. Hydrostatic high drag regime at $t^* = 6$: (a) potential temperature and (b) vertical velocities with contour interval of 200 cm s^{-1}. The dashed lines indicate negative values and regions where the mixing coefficient for momentum is larger than 50 m^2 s^{-1} are shaded in the potential temperature plot.

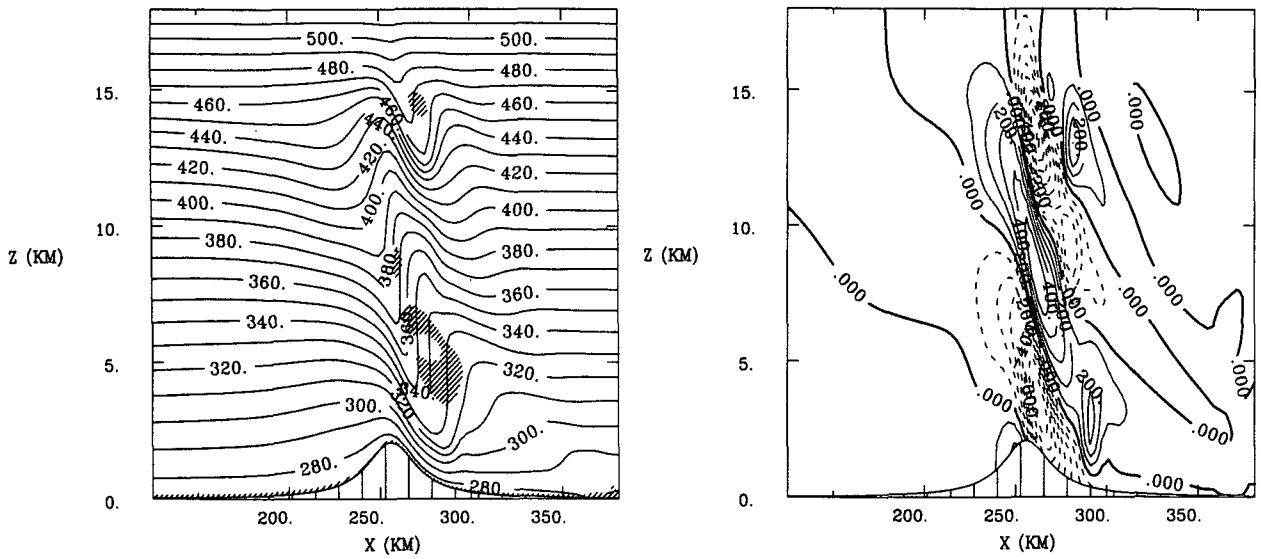

FIG. 11. As in Fig. 10 but at $t^* = 8$.

corresponding value (13.7) of the previous case. However, a trend for the stabilization of the flux from the low levels to a value close to 0.98 is clearly evident in Fig. 4. Also, most of the hydrostatically normalized drag values appear to be closer to unity because the flow is characterized by a larger nondimensional horizontal scale $a^* = Na/U$.

2) LINEAR BUT LESS STABLE CASES

The model is now uniformly initialized with $U_0 = 16$ m s^{-1} and $N = 0.01$ s^{-1}, using a temperature profile of the form $T(z) = T_0[e^{Sz} + (\alpha/H_T S)(1 - e^{Sz})]$, where H_T is the isothermal height scale and $S = N^2/g$. The vertical structure of this case should correspond closely to that of the first isothermal simulation since both the stability and wind speed have been reduced by one-half. The highest temperature of the initial state is taken as $T_0 = T^* = 273.16$ K. The normalized vertical flux of momentum (Fig. 5) reaches its nominal value 0.99 at low levels, but the final profiles appear less vertical than in Fig. 2. This may be due to the fact that now a part of the solution depends upon larger explicit terms proportional to T' [Eqs. (15)–(17)] caused by notable differences between the isothermal reference profile T^* and the upstream stratification of the airflow. It is possible also that the sponge may still allow some downward reflection of wave energy. For instance, owing to a smaller vertical group velocity in this case, the absorption of momentum flux occurs in a much thinner layer at the base of the sponge layer (compare Fig. 2 to Fig. 5).

In order to explore the stability of the semi-implicit scheme, two additional experiments were run by shifting T^* by plus and minus 20 K while keeping constant U_0, T_0, and the top-sponge profile in the model. Examination of Figs. 6 and 7 indicates a slight degradation (and a small damped initial instability for the first profile at $t^* = 10$) of the model results when T^* is warmed, while the normalized vertical flux and drag are underestimated (0.93) when T^* is cooled by the same amount. These observations lead us to conclude that the semi-implicit scheme is still applicable when the reference state is very different from the ambient stratification, but increasing locally the difference between the actual and the reference fields will obviously be detrimental for canonical simulations with simply layered atmospheres. The results show that indeed the best compromise for T^* is to consider the warmest temperature of the whole domain of simulation as already suggested by Simmons et al. (1978).

3) NONLINEAR REGIME

The model is initialized with $N = 0.02$ s^{-1} and $U_0 = 32$ m s^{-1}; the mountain height is fixed at 800 m, giving $\hat{h} = Nh/U_0 = 0.5$. The nonlinear mountain wave solution is shown at $t^* = 100$ for U, w, and θ in Fig. 8. A more precise measure of the accuracy of the model solution is given in Fig. 9, where the vertical profiles of momentum flux are reproduced. Once again, the model solution seems stable and accurate in spite of the slightly wavy aspect of the flux that is attributed to the vertical interpolation of the local value of vertical momentum flux from model terrain-following coordinate to constant height surfaces for calculating the horizontal average flux. The steady state appears to have been achieved when the successive profiles (F, G, H) tend to be superimposed, but a careful examination of the drag values reported in the figure indicates that the so-

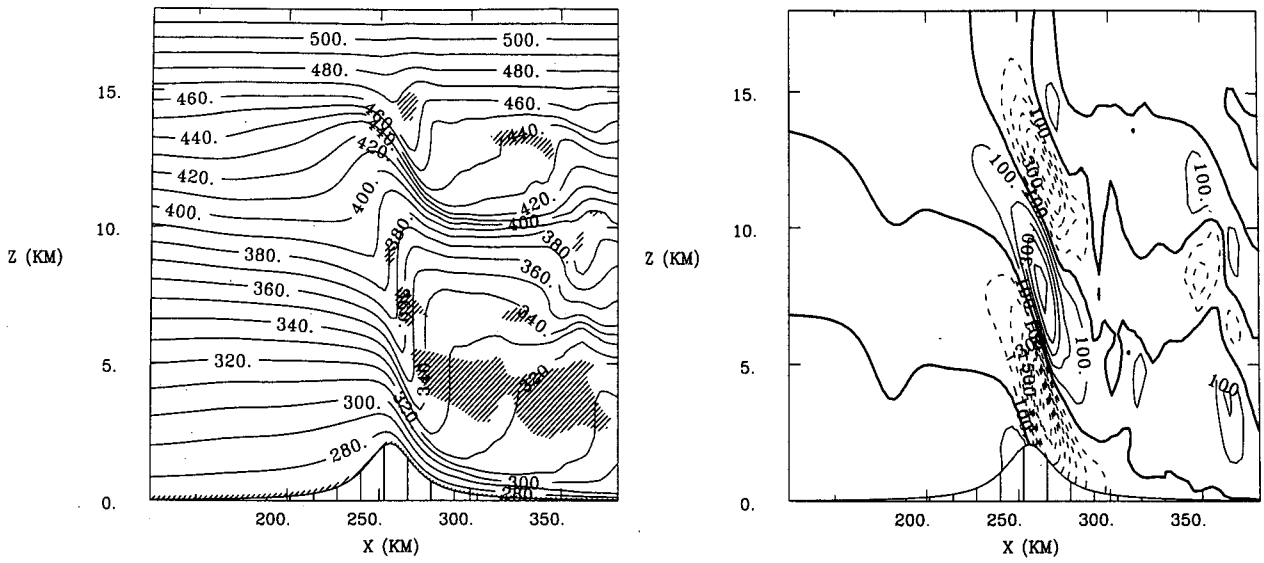

FIG. 12. As in Fig. 10 but at $t^* = 18$.

lution is slowly decaying. The model-computed surface drag reaches a value of about 1.15 and is very comparable to the first-order correction of Miles and Huppert (1969), which gives 1.11. However, it is worthwhile to mention that the model solution is sensitive to the position of the bottom of the damping layer with respect to the phase of the main wave, as noted by Klemp and Durran (1983).

4) HIGH DRAG REGIME

This test is an attempt to simulate a highly nonlinear case leading to a wave-breaking phenomena. We impose to an isothermal airflow ($U_0 = 30$ m s^{-1}) the crossing of a high mountain of 2240 m. The resulting $h^* = Nh/U = 1.4$ is approximately twice the critical value of h^* for which a flow transition is expected (Peltier and Clark 1979). For this simulation, the mountain grows linearly with time until $t^* = 4$, where it achieves its nominal value. As wave breaking is likely to occur, a simple first-order subgrid-scale mixing parameteriza-

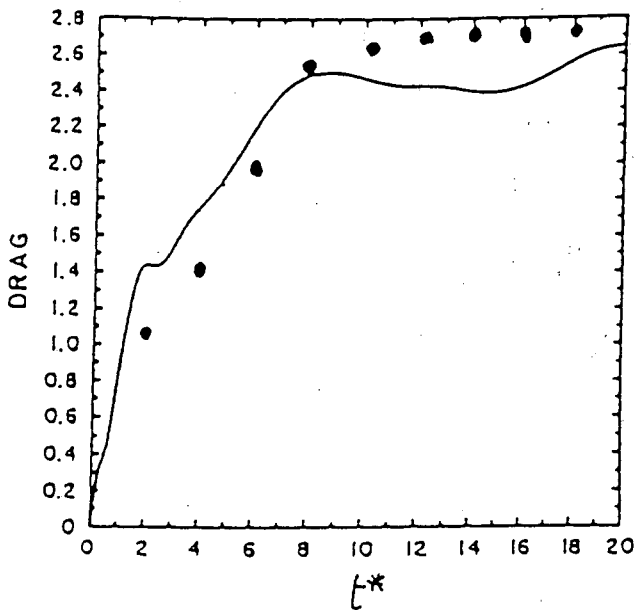

FIG. 13. Normalized pressure drag for the high-drag regime. The solid curve refers to the model results of Durran (1986), while the dots correspond to results of this study.

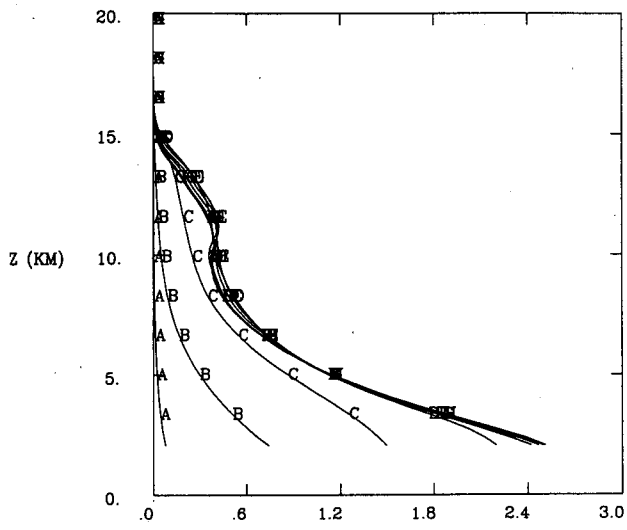

FIG. 14. Normalized vertical flux of momentum for the high-drag regime. The curve labeled A is for $t^* = 2$ and so on up to $t^* = 18$ for curve labeled I.

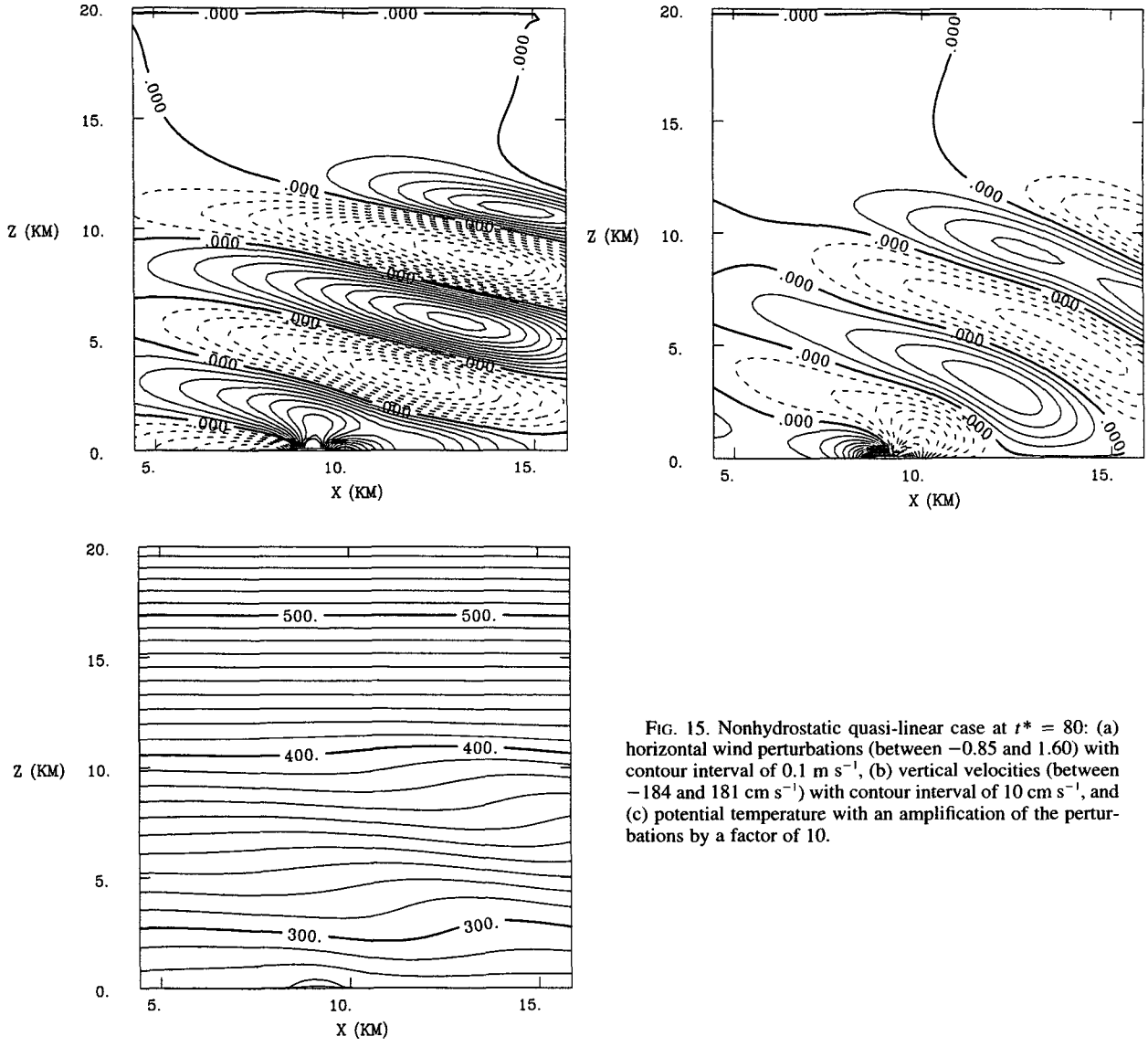

FIG. 15. Nonhydrostatic quasi-linear case at $t^* = 80$: (a) horizontal wind perturbations (between −0.85 and 1.60) with contour interval of 0.1 m s^{-1}, (b) vertical velocities (between −184 and 181 cm s^{-1}) with contour interval of 10 cm s^{-1}, and (c) potential temperature with an amplification of the perturbations by a factor of 10.

tion analogous to that used by Durran (1986) has been added to the model. The mixing terms acting on U, w, and T [through application of the scheme to the potential temperature θ and using the reversible transformation into $\theta = T(p_0/p)^{R/C_p}$] are added after each semi-implicit step. The generalized vertical velocity W [Eq. (6)] needs also to be recomputed after the mixing made on the U and w fields.

The phenomenology of the large amplification mechanism is examined with the isentropes and vertical velocities of the airflow at some selected times, that is, $t^* = 6$ (Fig. 10), $t^* = 8$ (Fig. 11), and $t^* = 18$ (Fig. 12). One can observe successively the rapid growth of the wave that first reaches its critical state at $t^* = 6$ (Fig. 10a), followed by the formation of the shooting flow in the lee slope (Fig. 11b) and its downstream displacement while the nonlinear wave remains well developed (Fig. 12). It is also apparent in Fig. 12 that the second wave aloft is breaking, although it is partly located in the lower levels of the absorbant. The resulting pressure drag is compared to that of Durran (1986) in Fig. 13. One can clearly see that shortly after $t^* = 8$ the airflow monotonically attains its asymptotic development with a surface drag value of about 2.7 times the linear value, which is 10% greater than that found by Durran at the same time; at $t^* = 18$, however, both drag values compare well. The vertical profile of momentum flux (Fig. 14), corroborates the steadiness of the flow after $t^* = 8$. Unlike the previous cases, the flux is divergent because the transport of momentum is now balanced by the subgrid-scale mixing (redistribution) term and the large

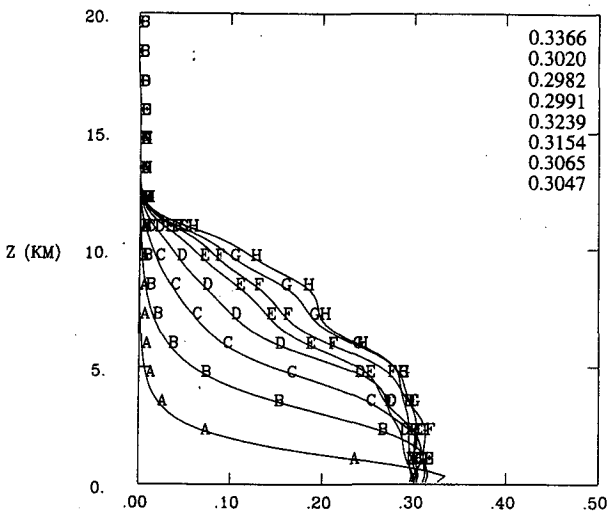

FIG. 16. As in Fig. 2 but for the nonhydrostatic quasi-linear case.

downstream transport of momentum associated with the transient flow.

c. *Nonhydrostatic waves*

Up to now the model has been tested for a hydrostatic flow configuration for which the orographically excited internal waves can freely propagate upward because their spectrum contains mostly low horizontal wavenumbers relative to the hydrostatic vertical wavenumber of the atmosphere N/U. Thus, when the horizontal scale of the mountain is decreased, the high wavenumber part of the mountain-wave spectrum can exceed N/U and cause these wavenumbers to become evanescent. To simulate such a situation, we still choose an isothermal atmosphere but with $a^* = 2/3$ and $h^* = 2/15$. The horizontal resolution is given by $\Delta x = a/5 = 100$ m and the timestep of 4 s corresponds to a Courant number of 0.56 as $U = 14$ m s^{-1}. The base of the top-sponge layer is still at $Z_{min} = 10$ km since we wish to resolve two vertical wavelengths only.

The results of the simulation are shown at $t^* = 80$. Both the horizontal wind perturbation (Fig. 15a) and the vertical wind velocity (Fig. 15b) reveal the characteristic downstream propagation of the main wave with height. This feature is also apparent on the potential temperature plot (Fig. 15c) where the two resolved buoyancy perturbations are shifted downstream as expected. A more quantitative view of the quality of the simulation can be seen by looking at the vertical flux of momentum normalized by its hydrostatic value (Fig. 16). The model solution clearly approaches its steady state ($t^{**} = 6$) in the low levels where the normalized value of the drag ($\sim$0.3) is in agreement with the theoretical value derived by Klemp and Lilly (1980). By $t^* = 80$, the solution aloft has clearly not yet reached a steady state, and the momentum flux is still divergent there.

d. *Potential flow*

As the mountain width is further reduced, the flow regime becomes supercritical (the equivalent Froude number U/Nh is large enough compared to 1). The atmosphere is now fully opaque to the propagation of internal gravity waves, and the wave drag is nearly zero. This case can be well simulated with the numerical model by setting $a^* = h^* = 0.12$. The highest level of the domain H is dropped down to 5 km (and $Z_{min} = 2.5$ km) since the vertical flow perturbations scales as h, approximately. The quasi-symmetrical flow patterns shown in Fig. 17a (horizontal wind speed), Fig. 17b (vertical velocity), and Fig. 17c (potential temperature) are good indicators of the absence of internal wave activity.

e. *Nonlinear nonhydrostatic regime*

Miles and Huppert (1968) derived analytical solutions for flows over a semicircular obstacle. They found that the value $Nh/U_0 = 1.27$ would lead to the onset of wave overturning. This flow configuration is a severe test for the model because of the steepness of the lower boundary condition.

The model is run for an isothermal atmosphere with $U_0 = 13.275$ m s^{-1} and with $a = h = 3\Delta x$ ($\Delta x = 300$ m). The time step is very small (1 s) because of the Eulerian vertical advection limitation, a possible reinforcement of explicit acoustic modes by the slope factors G_1/G_0 in Eq. (1) and the need to approach rather slowly the unstable regime. There are still 81 equidistant levels, but the vertical resolution has been adjusted in such a way that the upper rigid lid is moved up to $H = 40$ km. Half of the top levels are reserved for the absorbing layer.

In Fig. 18 we have plotted a close-up view of the horizontal wind field perturbation taken at $t = 1000$ s. The semicircular mountain shape is poorly reproduced, but the maximum numerical slope (2.236) is high indeed and leads to relatively high vertical velocities (not shown) of about 12.8 m s^{-1} (-28 m s^{-1}) on the upwind (downwind) slope. One can easily notice the downstream slant axis of the main nonhydrostatic wave with a first trough where the horizontal flow is nearly stagnant. At the same horizontal location but slightly below, the isentropes are vertical (Fig. 19a). This last picture bears some resemblance with the analytical solution of Miles and Huppert (1968) reproduced for comparison in Fig. 19b, although the downstream displacement of the unstable wave is less. This discrepancy is also noticeable in the Fig. 13 of Sharman et al. (1988), who attempted to compare their model with an analytical solution for a semielliptical mountain shape. Also as indicated by Sharman et al., the upper-level

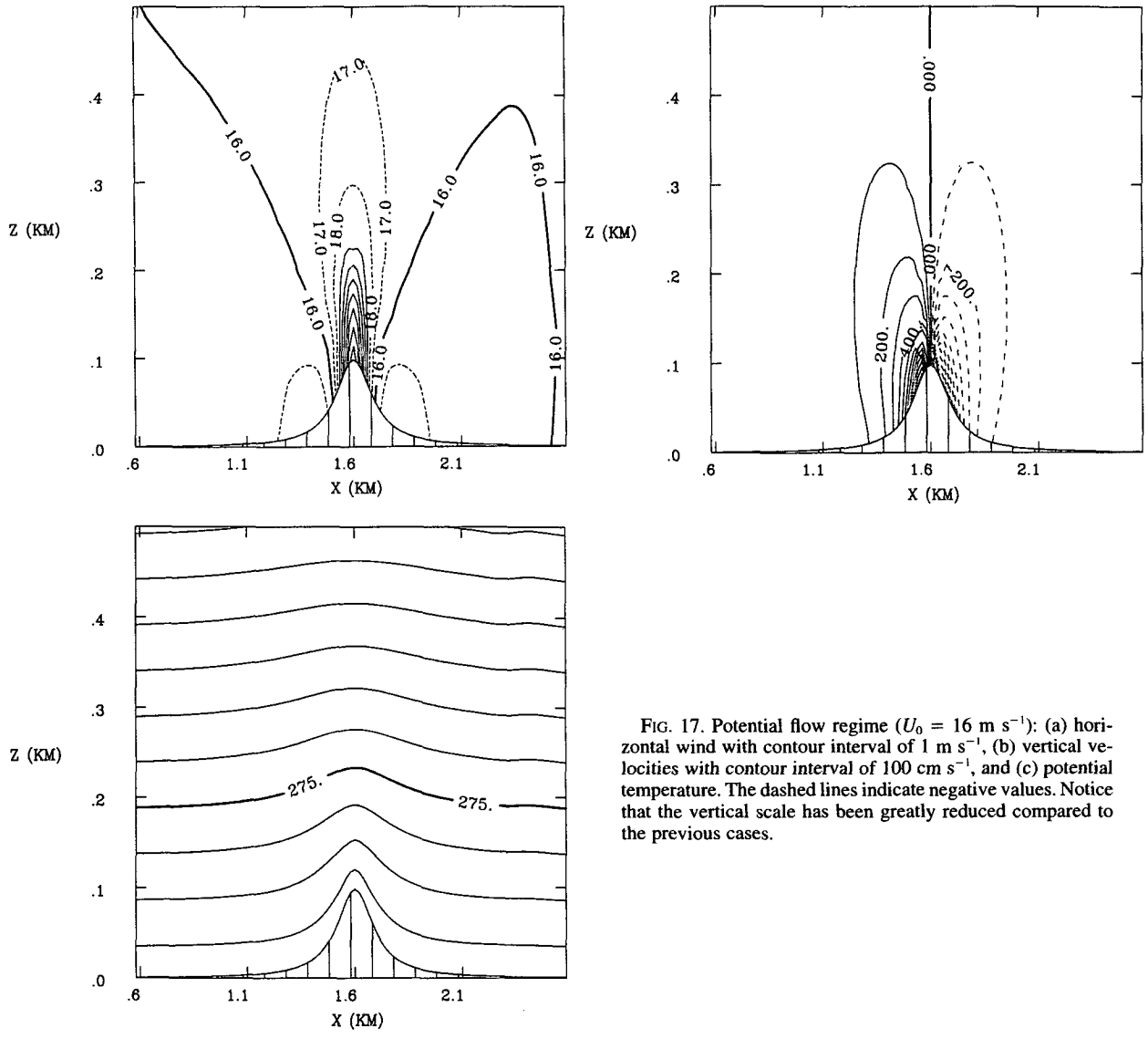

FIG. 17. Potential flow regime (U_0 = 16 m s^{-1}): (a) horizontal wind with contour interval of 1 m s^{-1}, (b) vertical velocities with contour interval of 100 cm s^{-1}, and (c) potential temperature. The dashed lines indicate negative values. Notice that the vertical scale has been greatly reduced compared to the previous cases.

development of the wave cannot be well simulated because wave breaking will occur in the model before it reaches its steady-state solution.

The ratio between the model-computed pressure drag and the corresponding analytical value $D^*(\pi/3)\rho U_0^2 a/a^{*3}$ [obtained from (3.10) of Miles and Huppert (1968) and with $D^* \sim 0.66$ as suggested by their Fig. 2] is 0.95. This value should be considered as acceptable in view of the numerical difficulty of running this test.

5. Conclusions

The semi-implicit semi-Lagrangian technique used to integrate a fully compressible nonhydrostatic model designed to simulate internal gravity waves induced by a variety of flows over canonically shaped topographies seems reliable. Some high-resolution simulations of simple linear hydrostatic flows and other tests performed for nonlinear and steep mountains highlight the good accuracy of the temporal scheme and the stability of the semi-Lagrangian advection scheme. It is worth emphasizing that no additional wave damping, filtering, or numerical diffusion was necessary for the model solution to achieve acceptable steady-state solutions other than the sponges below the lid and lateral boundaries of the computational domain and the usual time filter required by the time discretization of the model over three successive time steps.

The semi-implicit separation between the linear terms and the remaining (generally nonlinear) forc-

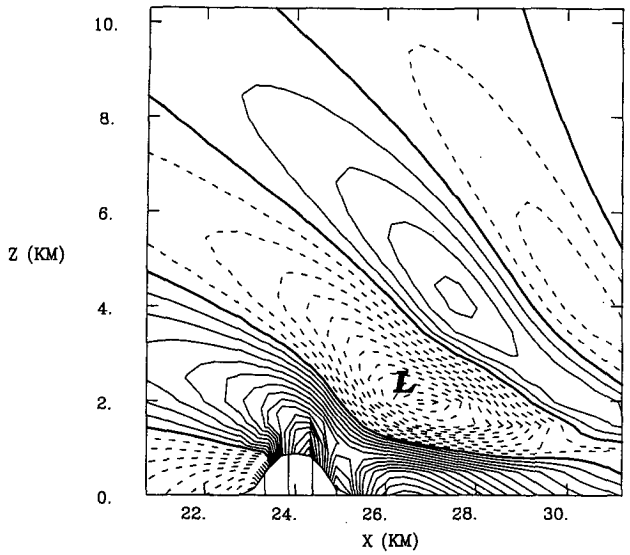

FIG. 18. Horizontal wind speed deviations from the basic state at $t = 1000$ s for a nonhydrostatic nonlinear flow over a semicircular mountain. The contour interval is 1 m s^{-1} and the dashed contours delimitate regions where the flow decelerates. The location of the minimum wind speed is marked by L.

ings gives the best results when the chosen model reference state has a stratification close to that of the ambient flow. This observation hints at monitoring the reference state, which in some circumstances could be nonisothermal for less stable flow conditions. However, in the case of nonlinear simulations with widely inhomogeneous field perturbations, the arguments of Simmons et al. (1978) in favor of a stable (isothermal) reference state are fully relevant as illustrated by the bubble convection experiments made by Robert (1993).

Most of the model response and accuracy depends on the semi-Lagrangian scheme that averages the linear gravity waves and the other explicit terms along parcel trajectories. The deficiency of the semi-Lagrangian technique when Courant numbers are larger than unity in the case of gravity wave problems is fully understandable as a consequence of the along trajectory averaging of the terms responsible for the gravity wave generation. As the Courant number increases, the highest horizontal wavenumbers are increasingly damped and so do not fully participate to the model solution (Héreil and Laprise 1994). A better averaging procedure could be obtained by changing to a three-point averaging operator taking opportunity of the model discretization over three successive time steps. The importance of using a higher-order averaging operator was already stressed by Smolarkiewicz and Pudykiewicz (1992), although their results did not improve when using their so-called extended trapezoidal scheme, perhaps because their model is built with an explicit scheme. The last point concerning the semi-Lagrangian advection scheme is the possibility to include with a minimal effort both monotone (Bermejo and Staniforth 1992) and conservative (Priestley 1992) properties to the scheme. However, some preliminary tests (not reported here) do not show a significant improvement of the model solution when the constraint for monotonicity is activated.

In conclusion, the original scheme developed by Robert and coworkers (Tanguay et al. 1990; Denis 1990; Bergeron et al. 1994) seems accurate and also efficient for mesoscale flows. The implicit numerical filtering of elastic modes and the treatment of the linear

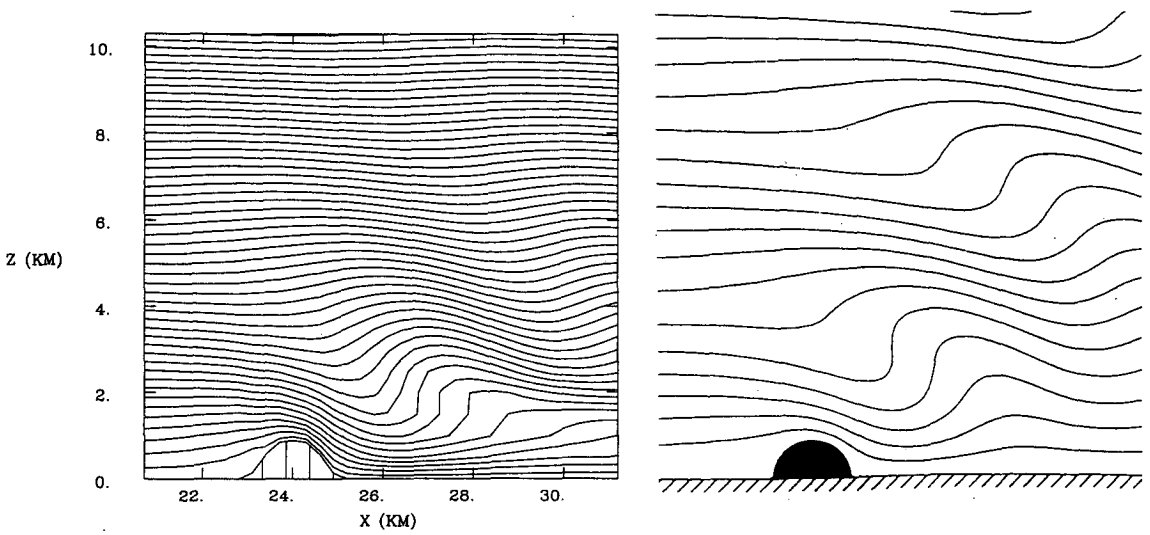

FIG. 19. Nonhydrostatic nonlinear case with a semicircular mountain: (a) model-predicted potential temperature and (b) analytical solution of Miles and Huppert (1968).

gravity waves by combining an implicit and a Lagrangian scheme is an elegant way to avoid some problems inherent to split-process techniques (Skamarock and Klemp 1992). It is noteworthy that even though an accurate representation of internal gravity waves does not allow the use of very long time steps corresponding to Courant numbers greater than about 0.5, the semi-implicit semi-Lagrangian technique is nevertheless reliable for simulating small-scale forcing phenomena with time steps 2.5–4 times larger than those commonly used in Eulerian split-explicit compressible or anelastic models.

In forthcoming experiments with MC2, the testing of the model will be extended to thermally forced flows with moving gravity waves and to the simulation of 2D multilayered flows leading to highly nonlinear amplification of trapped lee waves as observed in some real cases. In order to take advantage of the weak diffusion of the semi-Lagrangian advection, we also plan to investigate the low–Froude number regime for flows around 3D isolated obstacles.

Acknowledgments. The authors wish to express their profound respect to the memory of Prof. A. Robert for his unfailing faith in the semi-implicit semi-Lagrangian methods in fluid mechanics. We thank Dr. J. Klemp for his pertinent comments and suggestions regarding the overall scheme efficiency, which helped us to further progress into the evaluation of the numerical technique. We also gratefully acknowledge Y. Chartier and M. Desgagné (RPN, Montréal, Canada) for their important programming effort, M. Tanguay (RPN, Montréal, Canada) for her advices on the ADI method, and G. Bergeron (UQAM, Montréal, Canada) for his meticulous work in documenting the model. Joël Stein (Météo-France) is thanked for his pertinent remarks on the first model results, as well as J.-Martial Cohard (LA, Toulouse, France) for performing the highly nonlinear simulations. Two of us (J.-P. Pinty and E. Richard) were funded by ATP PATOM. The simulations were partially run on the Cray2 of the Centre de Calcul Vectoriel pour la Recherche and on the C98 of the Institut pour le Développement de la Recherche en Informatique Scientifique (both in Palaiseau, France).

REFERENCES

Anthes, R. A., and T. T. Warner, 1978: Development of hydrodynamic models suitable for air pollution and other mesometeorological studies. *Mon. Wea. Rev.*, **106**, 1045–1078.

Bergeron, G., and Coauthors, 1994: Formulation of the Mesoscale Compressible Community (MC2) model. Report of the Cooperative Centre for Research in Mesometeorology, 165 pp. [Available from R. Laprise, Département de Physique, Université du Québec à Montréal, PO Box 8888, Stn "Downtown," Montreal, Quebec, Canada, H3C 3P8.]

Bermejo, R., and A. Staniforth, 1992: The conversion of semi-Lagrangian advection schemes to quasi-monotone schemes. *Mon. Wea. Rev.*, **120**, 2622–2632.

Clark, T. L., 1977: A small-scale dynamic model using a terrain following coordinate transformation. *J. Comput. Phys.*, **24**, 186–215.

Coiffier, J., P. Chapelet, and N. Marie, 1987: Study of various quasi-Lagrangian techniques for numerical models. *Proc. of ECMWF Workshop on Techniques for Horizontal Discretization in Numerical Weather Prediction Models*, 377 pp.

Cullen, M. J. P., 1990: A test of a semi-implicit integration technique for a fully compressible nonhydrostatic model. *Quart. J. Roy. Meteor. Soc.*, **116**, 1253–1258.

Denis, B., 1990: Introduction de la topographie dans un modèle atmosphérique non-hydrostatique. *Mémoire de maîtrise U.Q.A.M.*, 121 pp. [Available from R. Laprise, Département de Physique, Université du Québec à Montreal, PO Box 8888, Stn "Downtown", Montreal, Quebec, Canada, H3C 3P8.]

Durran, D. R., 1986: Another look at downslope windstorms. Part I: The development of analogs to supercritical flow in an infinitely deep, continuously stratified fluid. *J. Atmos. Sci.*, **43**, 2527–2543.

——, 1989: Improving the anelastic approximation. *J. Atmos. Sci.*, **46**, 1453–1461.

Gal-Chen, T., and R. Somerville, 1975: On the use of a coordinate transformation for the solution of the Navier–Stokes equations. *J. Comput. Phys.*, **17**(2), 209–228.

Haltiner, G. J., and R. T. Williams, 1980: *Numerical Prediction and Dynamic Meteorology*. John Wiley and Sons, 477 pp.

Héreil, P., and R. Laprise, 1994: Sensitivity of internal gravity waves solutions to the time step of a semi-implicit semi-Lagrangian nonhydrostatic model. *Mon. Wea. Rev.*, submitted.

Klemp, J. B., and D. K. Lilly, 1978: Numerical simulation of hydrostatic mountain waves. *J. Atmos. Sci.*, **35**, 78–107.

——, and ——, 1980: Mountain waves and momentum flux. *Orographic Effects in Planetary Flows, ICSU/WMO*, GARP Publ. Ser., No. 23, 116–141.

——, and D. R. Durran, 1983: An upper boundary condition permitting internal gravity wave radiation in numerical mesoscale model. *Mon. Wea. Rev.*, **111**, 430–444.

Lipps, F., and R. Hemler, 1982: A scale analysis of deep moist convection and some related numerical calculations. *J. Atmos. Sci.*, **39**, 2192–2210.

Miles, J. W., and H. E. Huppert, 1968: Lee waves in a stratified flow. Part 2. Semi-circular obstacle. *J. Fluid Mech.*, **33**, 803–814.

——, and ——, 1969: Lee waves in a stratified flow. Part 4. Perturbation approximations. *J. Fluid Mech.*, **35**, 487–525.

Ogura, Y., and N. Phillips, 1962: Scale analysis of deep and shallow convection in the atmosphere. *J. Atmos. Sci.*, **19**, 173–179.

Peltier, W. R., and T. L. Clark, 1979: The evolution and stability of finite-amplitude mountain waves. Part II: Surface wave drag and severe downslope windstorms. *J. Atmos. Sci.*, **36**, 1498–1529.

Pielke, R. A., 1974: A three-dimensional numerical model of the sea breezes over south Florida. *Mon. Wea. Rev.*, **102**, 115–139.

Priestley, A., 1992: A quasi-conservative version of the semi-Lagrangian advection scheme. *Mon. Wea. Rev.*, **121**, 621–629.

Robert, A., 1966: The integration of a low order spectral form of the primitive meteorological equations. *J. Meteor. Soc. Japan*, **44**, 237–245.

——, 1981: A stable numerical integration scheme for the primitive meteorological equations. *Atmos.-Ocean*, **19**, 35–46.

——, 1993: Bubble convection experiments with a semi-implicit formulation of the Euler equations. *J. Atmos. Sci.*, **50**, 1865–1873.

——, T. L. Yee, and H. Ritchie, 1985: A semi-Lagrangian and semi-implicit numerical integration scheme for multilevel atmospheric models. *Mon. Wea. Rev.*, **113**, 388–394.

Sharman, R. D., T. L. Keller, and M. G. Wurtele, 1988: Incompressible and anelastic flow simulations on numerically generated grids. *Mon. Wea. Rev.*, **116,** 1124–1136.

Simmons, A. J., B. J. Hoskins, and D. M. Burridge, 1978: Stability of the semi-implicit method of time integration. *Mon. Wea. Rev.*, **106,** 405–412.

Skamarock, W. C., and J. B. Klemp, 1992: The stability of time-split numerical methods for the hydrostatic and the nonhydrostatic elastic equations. *Mon. Wea. Rev.*, **120,** 2109–2126.

Smolarkiewicz, P. K., and J. A. Pudykiewicz, 1992: A class of semi-Lagrangian approximations for fluids. *J. Atmos. Sci.*, **49,** 2082–2096.

Staniforth, A., and J. Côté, 1991: Semi-Lagrangian integration schemes for atmospheric models—A review. *Mon. Wea. Rev.*, **119,** 2206–2223.

Tanguay, M., A. Robert, and R. Laprise, 1990: A semi-implicit semi-Lagrangian fully compressible regional forecast model. *Mon. Wea. Rev.*, **118,** 1970–1980.

——, E. Yakimiw, H. Ritchie, and A. Robert, 1992: Advantages of spatial averaging in semi-implicit semi-Lagrangian schemes. *Mon. Wea. Rev.*, **120,** 113–123.

Tapp, M. C., and P. W. White, 1976: A nonhydrostatic mesoscale model. *Quart. J. Roy. Meteor. Soc.*, **102,** 277–296.

Tokioka, T., 1978: Some considerations on vertical differencing. *J. Meteor. Soc. Japan*, **44,** 25–43.